



Swansea University
Prifysgol Abertawe



Cronfa - Swansea University Open Access Repository

This is an author produced version of a paper published in:

Advanced Materials

Cronfa URL for this paper:

<http://cronfa.swan.ac.uk/Record/cronfa40905>

Paper:

Burton, M., Liu, T., McGettrick, J., Mehraban, S., Baker, J., Pockett, A., Watson, T., Fenwick, O. & Carnie, M. (2018). Thin Film Tin Selenide (SnSe) Thermoelectric Generators Exhibiting Ultralow Thermal Conductivity. *Advanced Materials*, 30(31), 1801357

<http://dx.doi.org/10.1002/adma.201801357>

14/8/18 copyright line corrected on this version. RK

This item is brought to you by Swansea University. Any person downloading material is agreeing to abide by the terms of the repository licence. Copies of full text items may be used or reproduced in any format or medium, without prior permission for personal research or study, educational or non-commercial purposes only. The copyright for any work remains with the original author unless otherwise specified. The full-text must not be sold in any format or medium without the formal permission of the copyright holder.

Permission for multiple reproductions should be obtained from the original author.

Authors are personally responsible for adhering to copyright and publisher restrictions when uploading content to the repository.

<http://www.swansea.ac.uk/library/researchsupport/ris-support/>

Thin Film Tin Selenide (SnSe) Thermoelectric Generators Exhibiting Ultralow Thermal Conductivity

Matthew R. Burton, Tianjun Liu, James McGettrick, Shahin Mehraban, Jenny Baker, Adam Pockett, Trystan Watson, Oliver Fenwick, and Matthew J. Carnie*

Tin selenide (SnSe) has attracted much attention in the field of thermoelectrics since the discovery of the record figure of merit (ZT) of 2.6 ± 0.3 along the b -axis of the material. The record ZT is attributed to an ultralow thermal conductivity that arises from anharmonicity in bonding. While it is known that nanostructuring offers the prospect of enhanced thermoelectric performance, there have been minimal studies in the literature to date of the thermoelectric performance of thin films of SnSe. In this work, preferentially orientated porous networks of thin film SnSe nanosheets are fabricated using a simple thermal evaporation method, which exhibits an unprecedentedly low thermal conductivity of $0.08 \text{ W m}^{-1} \text{ K}^{-1}$ between 375 and 450 K. In addition, the first known example of a working SnSe thermoelectric generator is presented and characterized.

In 2014, an estimation of waste heat from industrial sources found that in the UK alone, 48 TWh yr^{-1} of energy is lost as waste heat, corresponding to around a sixth of overall industrial energy usage.^[1] Harvesting this wasted energy could contribute to energy efficiency targets, helping to reduce the need for fossil fuels, causing a reduction in greenhouse gas emissions and helping to tackle climate change. If only 1% of the industrial

waste heat could be harnessed, this would equate to a reduction of 0.25 Tg yr^{-1} of CO_2 emissions.^[2] Thermoelectric generators are solid state devices that require no maintenance, are highly reliable, and offer a route of energy recovery by exploiting temperature gradients generated by waste heat. Bulk material thermoelectric generators (TEGs) have applications to harvest waste heat from industry or a vehicle's exhaust.^[3] Thin film TEGs have the potential to power wireless sensors (in medicine, defense, internet of things, fashion, sport) or be used as thin film thermoelectric coolers.^[4]

In the field of thermoelectrics, the ability of materials to harvest heat energy is compared by the figure of merit (ZT),

see Equation (1). The higher a ZT value, the more efficient a material is at harvesting heat energy and converting it into usable electrical energy.

$$ZT = \frac{S^2 \sigma}{\kappa} T \quad (1)$$

where S is the Seebeck coefficient (V K^{-1}), σ the electrical conductivity (S m^{-1}), and κ the thermal conductivity ($\text{W m}^{-1} \text{ K}^{-1}$). T is the temperature of the material (K).^[5] The transport characteristics depend on interrelated material properties,^[6] thus optimizing one variable conflicts with another. One such example is Wiedemann–Franz law, which states the ratio of the electronic component of thermal conductivity (κ_e) to σ is proportional to temperature. This means an increase in σ yields an increase in κ , and limits the tuning of thermal conductivity to the lattice component, κ_l ($\kappa = \kappa_e + \kappa_l$). Due to these interrelated material properties, ZT had been stuck at a value of around 1 since the 1950s.^[7] In 1993, however, Hicks and Dresselhaus theorized that reduced dimensionality offers strategies to uncouple the transport characteristics,^[8,9] for example, lowering the Lorenz number (L), thus lowering thermal conductivity more than electrical conductivity ($\kappa_e = L \cdot T \cdot \sigma$). Nanostructures also allow for improved thermoelectric performance due to more severe thermal boundary resistances than electronic. This increases the σ/κ ratio by lowering the lattice component of thermal conductivity (κ_l). This can lead to increased ZT values for nanostructured materials relative to bulk values, which has been a significant focus of thermoelectrics research in recent years.^[10,11]

Lead telluride and bismuth telluride and their respective alloys have been the most studied materials for mid-temperature and room temperature applications in thermoelectrics, respectively, since the 1950s, when they were shown to produce

Dr. M. R. Burton, Dr. J. McGettrick, Dr. J. Baker, Dr. A. Pockett, Prof. T. Watson, Dr. M. J. Carnie
SPECIFIC

Materials Research Centre
College of Engineering
Swansea University
Bay Campus, Swansea SA1 8EN, UK
E-mail: m.j.carnie@swansea.ac.uk

T. Liu, Dr. O. Fenwick
School of Engineering and Materials Science
Queen Mary University of London
Mile End Road, London E1 4NS, UK

Dr. S. Mehraban
MACH1
Materials Research Centre
College of Engineering
Swansea University
Bay Campus, Swansea SA1 8EN, UK

 The ORCID identification number(s) for the author(s) of this article can be found under <https://doi.org/10.1002/adma.201801357>.

© 2018 The Authors. Published by WILEY-VCH Verlag GmbH & Co. KGaA, Weinheim. This is an open access article under the terms of the Creative Commons Attribution License, which permits use, distribution and reproduction in any medium, provided the original work is properly cited.

The copyright line for this article was changed on 1 Aug 2018 after original online publication.

DOI: 10.1002/adma.201801357

figures of merit (ZT) in the region of 1.^[5,7] Tellurium is however a rare element with an abundance in the earth's crust comparable of that to Pt ($1 \mu\text{g kg}^{-1}$).^[12] This leads there to be a need to use other materials to manufacture commercially viable thermoelectric devices outside of existing niche markets.

Tin selenide (SnSe) sparked much interest in the field of thermoelectrics when Zhao et al. reported an unprecedented ZT of 2.6 ± 0.3 at 923 K along the b -axis of a monocrystalline ingot.^[13] Bulk SnSe exhibits p -type behavior and a 2D layered structure with covalent bonding along the b - c -plane and weak van der Waals forces along the a -axis. This layered structure causes SnSe to exhibit strongly anisotropic transport properties, which are reflected in the lower ZT value of 0.8 ± 0.2 that was measured along the a -axis.^[13] This discovery was observed in single crystals formed at high temperature (1223 K) over several hours.

Doping of SnSe with elements such as Na ($ZT \approx 2$) and Bi ($ZT = 2.2$) has shown improved low temperature thermoelectric figures of merit, and the possibility of high performance n -type materials, respectively.^[14,15] These too were shown on single crystals however, with expensive, lengthy, and high temperature fabrication techniques which are unfavorable for commercial fabrication.

Since the discovery of the record ZT in single-crystal SnSe,^[13] studies on the thermoelectric performance of polycrystalline SnSe have been reported.^[16–24] Sassi et al. synthesized polycrystalline SnSe in quartz tubes and then densified by spark plasma sintering (SPS) and showed a peak ZT value of 0.5 at 823 K.^[16] Li et al. achieved a ZT of 0.58 at 773 K in textured SnSe polycrystals fabricated by the solvothermal synthesis (SS) followed by SPS.^[21] Shi et al. used the same technique but self-doped (SD) with Se to achieve a higher ZT of 1.36 ± 0.12 at 823 K.^[17] Wei et al. achieved a ZT of 0.8 at 800 K in polycrystalline SnSe with Na doping by using a combination of melting (M) and SPS.^[18] Li et al. achieved a ZT of 0.54 at 790 K by melting annealing (MA) and SPS.^[19] Fu et al. achieved a ZT of 0.92 at 873 K in highly textured polycrystalline SnSe created by zone melting (ZM),^[20] before using SPS to improve the ZT to ≈ 1.05 due to increased phonon scattering at the grain boundary. Morales Ferreira et al. achieved a ZT of 0.11 at 772 K by cold pressing (CP), then annealing SnSe powder.^[22] Chen et al. showed a ZT of up to 0.6 at 750 K in Ag-doped polycrystalline SnSe fabricated in hot quartz ampoules followed by hot pressing.^[23] Chere et al. prepared Na-doped polycrystalline SnSe using evacuated quartz tubes followed by ball milling and hot pressing,^[24] a peak ZT of ≈ 0.8 at 773 K was achieved. All these fabrication techniques presented in the literature require high temperature, lengthy fabrication times, and in most cases high pressure, techniques unfavorable for commercial fabrication.

Studies on nanostructured SnSe and SnSe-based materials to reduce the thermal conductivity (κ) are scarce in the literature. Suen et al. used pulsed laser glancing-angle deposition to grow thin films of SnSe, however did not report a ZT value due to measurements of electrical and thermal properties being on perpendicular planes.^[25] The lowest thermal conductivity measured is $0.120 \text{ W m}^{-1} \text{ K}^{-1}$, this is seen at 200 K.^[25] Ju et al. showed the fabrication of compressed pellets comprised of porous SnSeS nanosheets with a ZT of 0.12 at room temperature.^[26] Another technique that can be used to reduce the thermal conductivity of a material is the introduction of pores

into the structure. This has been successfully demonstrated in Si, Bi_2Te_3 , and manganese silicide to achieve improvements in ZT .^[27–29]

In this paper, we investigate the use of thermal evaporation to manufacture thin films of SnSe. Thermal evaporation is a relatively cheap and facile fabrication technique for thin film devices, in contrast to most SnSe fabrication techniques for thermoelectric applications already presented in the literature. While the thermal evaporation of SnSe has been conducted before in the literature,^[30] this was with a view to photovoltaic applications. Reactive evaporation was shown to produce a high Seebeck coefficient at low temperature,^[31] though the thermoelectric properties were poor at room temperature. In this study, we characterize the thermoelectric and material properties of SnSe thin films over a wide range of temperatures. Moreover, we demonstrate for the first time in the research literature, a thermally evaporated, thin film, SnSe thermoelectric generator. Perhaps even more interesting, we show that thermally evaporated SnSe thin films, due to their inherent nanostructuring, exhibit extremely low thermal conductivity, substantially below that of the a -axis of the single crystal.^[13] Such a low thermal conductivity is of use for the development of thermoelectric generators, but is also of interest to the development of other SnSe devices such as solar cells where heat dissipation is a concern.^[32]

To confirm the SnSe film, an X-ray diffraction (XRD) pattern for the SnSe powder (fully assigned in Figure S2a in the Supporting Information) and for a typical thermally evaporated SnSe thin film are shown in Figure 1. The peaks in these patterns can be assigned to the low temperature orthorhombic phase of SnSe which belongs to the $pnma$ space group (crystallography open database file number 1537675). While the SnSe powder diffraction pattern observed is similar to cold pressed SnSe powder,^[22] the thermally evaporated thin film has much larger (111) and (011) peak intensities compared to the other peak intensities. The Lotgering factors (see Equations (S1) and (S2) in the Supporting Information) for these peaks are

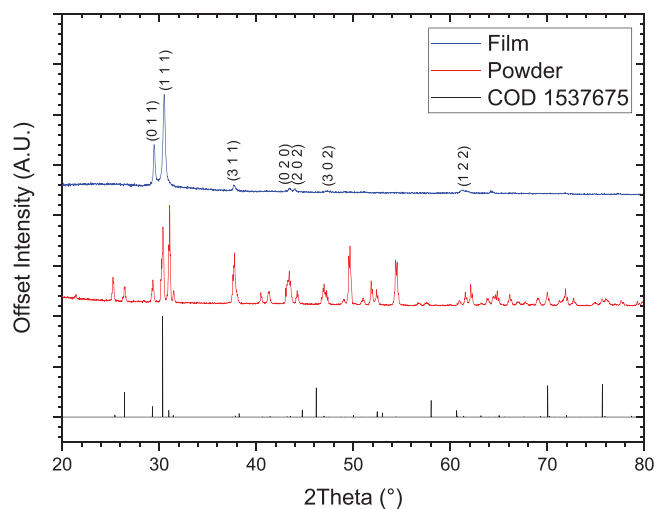


Figure 1. $2\theta/\theta$ XRD scans of SnSe powder (red line) and a thermally evaporated thin film (blue line). Peaks are assigned from the crystallographic open database (COD) file 1537675 (black line).

0.51 and 0.25, respectively,^[33] indicating preferred orientation along these planes on the substrate (in particular the (111) plane) which is the plane of measurement for Seebeck, electrical, and thermal conductivity.^[22] XRD of thinner films (Figure S2b, Supporting Information) also shows a preferred (111) orientation, indicating that this preferred orientation post thermal evaporation may be a result of energetic interactions with the glass substrate. These preferred orientation planes and the thinness of the thermally evaporated films explain the absence of peaks in the film which are shown in the powder.^[33]

Scanning electron microscopy (SEM) of the SnSe powder and the thermally evaporated SnSe thin films (Figure 2) show contrasting morphologies. While the grains of SnSe powder show a flat uniform surface morphology typical of a layered crystal (Figure 2a,b), the thermally evaporated films (Figure 2c) reveal a network of porous nanosheets. These nanosheets are formed throughout the film (Figure S3a–c, Supporting Information), further indicating that the nonporous structure may form because of an initial energetic preference interaction with the glass substrate which is maintained throughout the growth of the film. The nanosheets in these $\approx 1 \mu\text{m}$ thick films have a preferred orientation perpendicular to the substrate surface, in agreement with our orientated XRD observations. Nitrogen adsorption experiments on these films (Figure S4, Supporting Information) reveal a surface area of $22.2 \pm 0.1 \text{ m}^2 \text{ g}^{-1}$ calculated by Brunauer–Emmett–Teller (BET) analysis,^[34] and a pore size of 12.3 nm and a pore volume of $0.0683 \text{ cm}^3 \text{ g}^{-1}$ calculated by Barrett–Joyner–Halenda (BJH) analysis.^[35] This corresponds to a porosity of 42.3%. The energy-dispersive X-ray spectroscopy (EDX) pattern for the powder (Figure 2e) and for a film (Figure 2f) both show a high level of oxygen to be present; however, high levels of carbon are also observed, indicating contamination from the environment. This is not an unexpected result due to the small particle size of the powder and the porosity of the thin films, leaving ample compartments to trap environmental contamination. During thermal evaporation, a minimal pressure of 5 mPa persists inside the evaporation chamber. This pressure is of atmospheric air which would inevitably lead to minimal levels of SnO_2 and possibly $\text{Sn}(\text{SeO}_3)_2$ to be formed during evaporation,^[36,37] which could also account toward the slightly higher levels of O present in the films compared to the powder. The most significant cause for the observed increase in the oxygen concentration in the EDX spectrum of film compared to the powder however, is the observation of the underlying glass substrate as evident from the observation of 2.2 at% Si. This accounts for a minimum of a 4.4 at% increase in observed oxygen levels, with any further EDX disparities in oxygen levels between powder and the film being within the region of error for EDX.

Both Sn and Se doublets were examined by X-ray photoelectron spectroscopy (XPS). Quantifying the peaks suggests an excess of Sn in the film with a Sn:Se ratio of 1.7:1 compared to the expected SnSe composition of 1:1. The Sn $3d_{5/2}$ peak present at 485.6 eV (see Figure 2g) is consistent with SnSe, although the Se $3d_{5/2}$ peak is observed at an unusually low 53.3 eV (see Figure 2h). This compares to observed peak positions of 485.6–485.9 eV for Sn $3d_{5/2}$ and 53.6–53.7 eV for Se $3d_{5/2}$ peaks observed elsewhere for stoichiometric SnSe systems.^[21,26,36] This slight discrepancy in peak position for Se is attributed to the unusual stoichiometry of the present system,

with the Se remaining relatively electron dense compared to the Se(0) value of 55.2 eV.^[38] In both the cases, the sharp peaks with full width half maximum (FWHM) $< 1 \text{ eV}$ indicate a single bonding environment with no evidence of a SnO_2 peak at 486.7 eV or a Se^{4+} peak in the region of 58–59 eV.^[36,39] Survey scans suggest that only a minimal 11% oxygen is present on the surface with 2 oxygen environments (Figure S5, Supporting Information) present. A small peak at 531.8 eV is attributed to organic oxides (4.5%) and another small peak at 530.1 eV being attributed to metal oxides (7.5%). The metal oxide only appears at a ratio of 1:7.4 Sn, therefore the observed Sn_xSe surface is not significantly oxidized. The level of observed oxygen in XPS is therefore consistent with EDX values within reasonable error.

In-plane thermoelectric characterization (Figure 3) shows that the thermally evaporated Sn rich SnSe films are p-type in nature, a result which is consistent with density functional theory calculations.^[40] The films exhibit Seebeck coefficients of a similar magnitude to those seen by Zhao et al. at room temperature.^[13] While in single-crystal SnSe, the Seebeck coefficient is seen to drop from ≈ 550 to $\approx 350 \mu\text{V K}^{-1}$ between 600 and 800 K,^[13] for thermally evaporated thin films, the Seebeck coefficient is $> 600 \mu\text{V K}^{-1}$ at room temperature, but drops to $\approx 140 \mu\text{V K}^{-1}$ by 600 K with the drop starting at 460 K. This drop is more pronounced and at lower temperatures compared to single-crystal SnSe. Electrical conductivity (Figure 3a) is seen to be lower than other polycrystalline SnSe examples in the literature at room temperature (Figure S6, Supporting Information),^[16–24] but shows a sharp increase above 450 K to reach similar levels. This leads to a lower power factor (Figure 3c) compared to other examples of polycrystalline SnSe.^[16–24] Interestingly, an unprecedentedly low in-plane thermal conductivity for SnSe is observed throughout the temperature profile (Figure 3b,d), which is at its lowest between 375 and 450 K at $0.08 \text{ W m}^{-1} \text{ K}^{-1}$. This is over a factor of 4 lower than the low-thermal conductivity *a*-axis of the single crystal at comparable temperatures, and a factor of 2.75 lower when comparing the lowest thermal conductivity values measured.^[13] This thermal conductivity is also a factor of 2.80 and 1.50 lower than any bulk polycrystalline and thin film SnSe examples, respectively, when comparing with their lowest thermal conductivity values measured.^[16–25] The thermal conductivity of a material is intrinsically comprised of the sum of two components, the electronic element from the charge carriers (κ_e) and the lattice element from the phonons (κ_l). Figure 3b shows that while a negligible amount of the decreased thermal conductivity can be attributed to a reduction in the electronic component (κ_e) due to the lower electrical conductivity ($\kappa_e = L \cdot T \cdot \sigma$, assuming $L = 1.5 \times 10^{-8} \text{ V}^2 \text{ K}^{-2}$),^[13] the majority of the reduction in thermal conductivity is a result of a significant decrease in the lattice component (κ_l). For comparison, the axis of single-crystal SnSe with the lowest thermal conductivity (*a*-axis) is included in Figure 3b. This reduction in thermal conductivity can be rationalized when observing the morphology of the films which comprises a network of nanosheets preferentially orientated perpendicular to the surface. Lotgering analysis shows that although there is some preferred orientation to the SnSe, thermal transport in plane is not dominated by any one of the *a*-, *b*-, or *c*-axes, and therefore cannot be said to be due to transport along the low thermal conductivity *a*-axis.

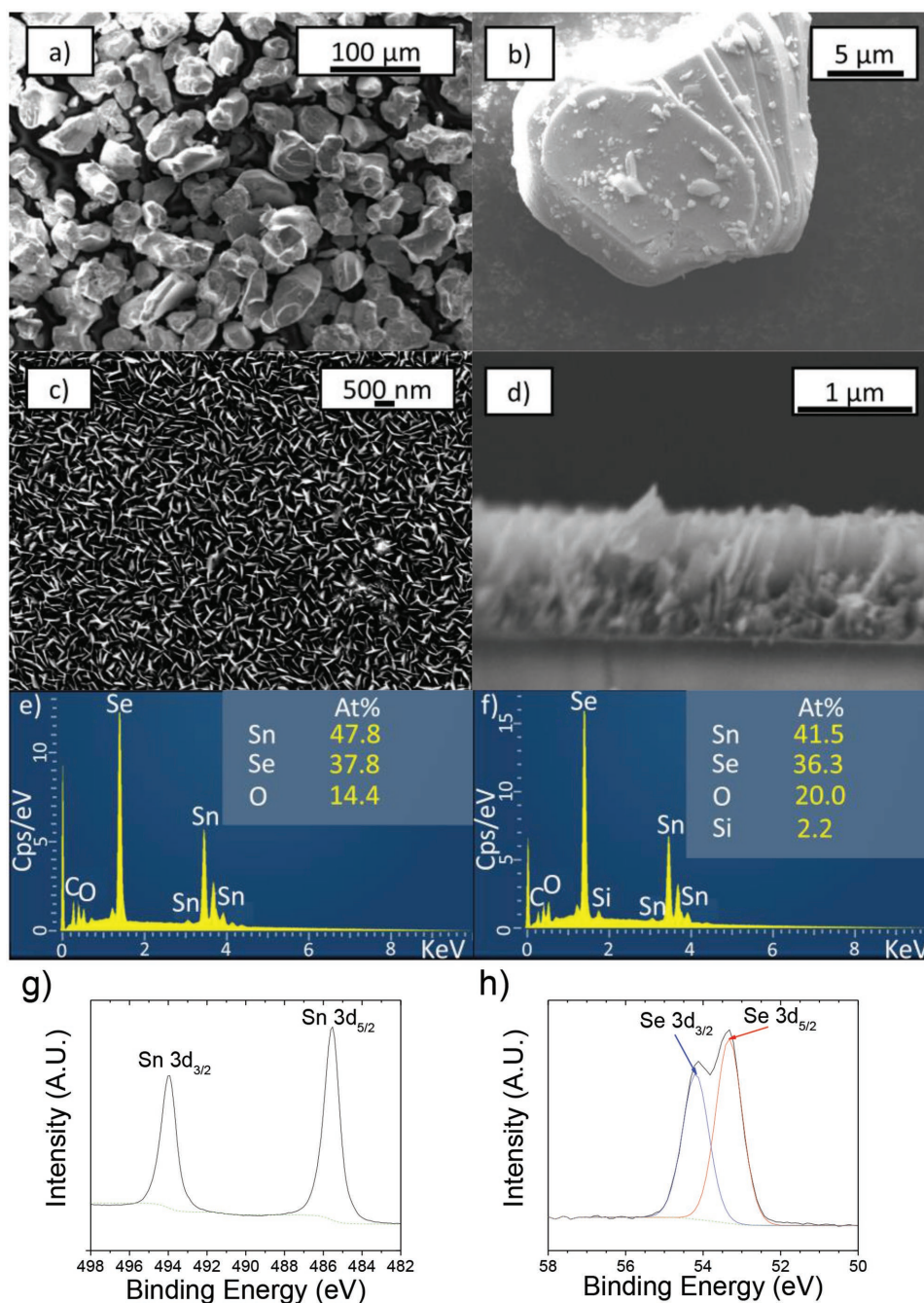


Figure 2. Morphology and compositional characterization of SnSe powder and thermally evaporated SnSe thin films. a,b) SEM of SnSe powder. c) SEM of surface morphology of a thermally evaporated SnSe film. d) Cross-section SEM of a thermally evaporated SnSe film. e) EDX of SnSe powder. f) EDX of a thermally evaporated SnSe film. g,h) XPS on a thermally evaporated film of Sn_xSe (showing Sn_{3d} and Se_{3d} peaks, respectively).

The low thermal conductivity is therefore driven by a combination of porosity and thermal resistance at sheet boundaries. From the SEM images (Figure 2c), we can estimate the thickness of the nanosheets in the network as 75 ± 10 nm. The phonon mean free path (MFP) in SnSe at 300 K is reported to be 5.6 nm along the *a*-axis, 4.9 nm along the *b*-axis, and 4.1 nm along the *c*-axis.^[41] Consequently, the MFP in all directions is smaller than dimensions of the nanosheets, and the phonons can exhibit diffusive transport inside the nanosheets with an

intrasheet thermal conductivity comparable to bulk values. However, when we introduce porosity in the nanosheet network, the phonons must choose a propagation pathway that does not cross the pores (Figure S7, Supporting Information) with a corresponding drop in thermal conductivity.^[42] Furthermore, thermal transport on these pathways may be limited by thermal boundary resistances (Kapitza resistances) caused by strong phonon scattering at the nodes of the nanosheet network. Interestingly, a transition is seen from ≈ 460 K where

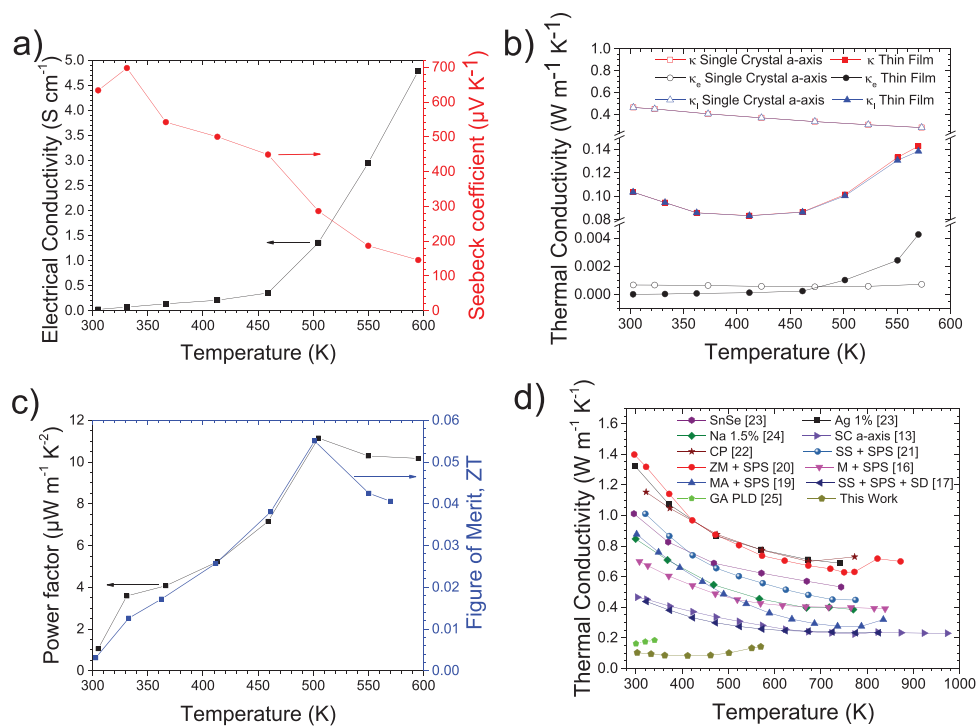


Figure 3. Thermoelectric characterization of thermally evaporated SnSe: a) electrical conductivity and Seebeck coefficient, b) κ of thermally evaporated SnSe compared to the a -axis of single-crystal SnSe, c) power factor and ZT , d) κ compared to other values for SnSe reported in the literature, where multiple values were reported, the smallest value was used.

the Seebeck coefficient decreases, while simultaneously the electrical and thermal conductivity increase. Differential scanning calorimetry (DSC) data (Figure S8, Supporting Information) rules out a phase change in this region but does show an acceleration of increase in energy at around this temperature, this may imply a thermal expansion that improves the contact at the grain boundaries. SEM of a film post measurement (Figure S3d, Supporting Information) reveals irreversible aggregation forming an interconnected nanostructure which by nature has fewer boundaries, which would explain the observed transition. It is also possible that the thermal and electrical contact at the boundaries between nanosheets is irreversibly modified during the measurements. This is consistent with the increase in electrical and thermal conductivities, while it is also known that electronic barriers can modulate the Seebeck coefficient.^[43] This is of interest to the thermoelectric community as it reveals that the thermal conductivity of SnSe can be reduced further than is observed in single-crystal SnSe.^[13] Due to the subdued power factor, the resultant peak ZT (0.055) seen in Figure 3c is lower than has been observed for bulk polycrystalline SnSe in the literature,^[16–24] however is the highest reported ZT for a thin film of SnSe above 70 K.^[25,31] We also note the simplicity of fabrication and shift in peak ZT to a lower temperature compared to bulk examples. The high surface area of these films also opens the possibility for molecular adsorption as a gas sensor,^[44] which could be self-powered.^[45] Furthermore, the network morphology opens up possibilities to tune ZT by fine modulation of transport barriers at the grain boundaries.

One route to morphological control is thermal annealing, as evident by the observation of nanostructure aggregation forming

an interconnected nanostructure seen post measurement in Figure S3d (Supporting Information). Seebeck and electrical analysis (Figure S9a, Supporting Information) shows that annealing of samples at 421 K has minimal effect on these properties. Annealing at 611 K (Figure S9b, Supporting Information) however is seen to have an irreversible effect resulting in Seebeck values which are an order of magnitude lower, the electrical conductivity is measured to be higher at <550 K, but lower afterward compared to nonannealed samples. Thermal annealing cycles (Figure S9c, Supporting Information) show incremental increases in thermal conductivity when heating to ≈ 470 K. Another route to control the morphology of the films is to dope the SnSe powder prior to evaporation. Figure S3e (Supporting Information) reveals successful morphology modification with 1.8% addition of Na_2Se by weight. There is seen to be a slight lowering of the Seebeck coefficient (Figure S9d, Supporting Information) and a more significant lowering of the electrical conductivity, while the thermal conductivity is seen to be increased by a factor of 2.5 (Figure S9e, Supporting Information).

We fabricated the first reported example of a SnSe thermoelectric generator by thermal evaporation through self-aligned shadow masks, in an approach that has been reported for bismuth telluride.^[46] The device can be seen in Figure 4a. The open-circuit voltage (V_0) and the short-circuit current (I_0) can be seen in Figure 4c and the resulting power output of the device (assuming maximum power = $V_0 I_0 / 4$ ^[47]) can be seen in Figure 4d. The devices were able to output 0.09 μW of power when the heater reached a temperature of 618 K. The performance dropped off when the hot-side temperature (T_H) was held in this region and inspection of the device at this time

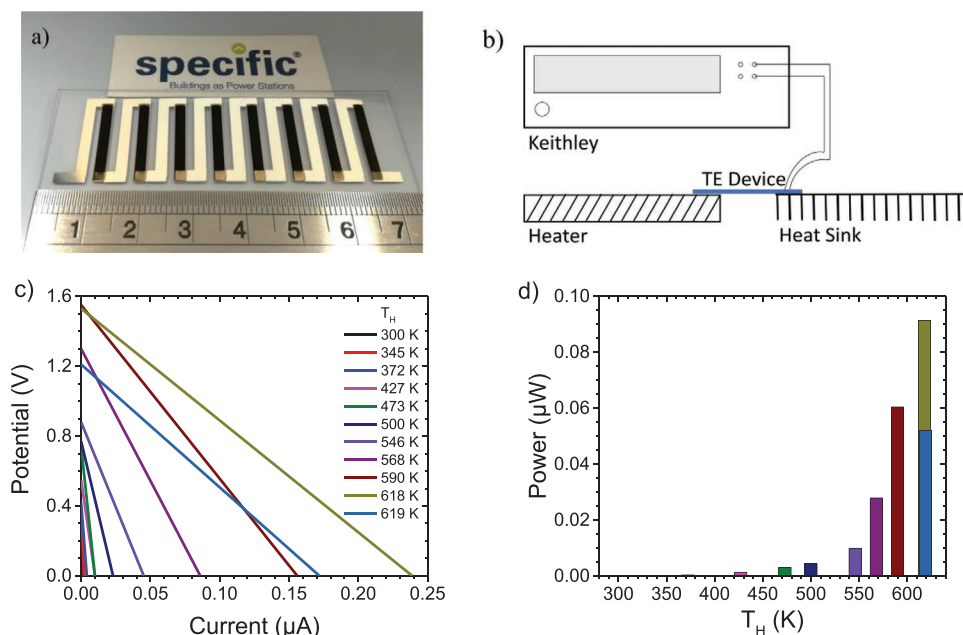


Figure 4. Thin film thermoelectric generator: a) image of device with ruler in cm for scale, b) schematic of device testing setup, c) the open-circuit voltage (V_0) and the short-circuit current (I_0) linearly connected, d) peak power outputs of the device (assuming maximum power = $V_0 I_0 / 4$).^[47]

revealed a discoloration of the SnSe legs. The cold-side temperature was not controlled. Therefore, the performance drop-off is explained by oxidation and loss of thermal gradient across the device during the measurement.

In conclusion, $\approx 1 \mu\text{m}$ thick films of SnSe were fabricated via a simple thermal evaporation method onto glass substrates. Seebeck coefficients comparable to that seen in bulk SnSe were measured and we demonstrate that these films exhibit unprecedented ultralow thermal conductivity of $0.08 \text{ W m}^{-1} \text{ K}^{-1}$ between 375 and 450 K. The electrical conductivity of the samples was also lowered compared to bulk SnSe, but the reduction in thermal conductivity was found to be primarily due to the reduction of the lattice component. We have demonstrated for the first time that thin film SnSe nanosheet morphology presents numerous phonon scattering sites due to the finite thickness of the sheets and at the junctions between the sheets. Knowledge of this ultralow thermal conductivity morphology is important for photovoltaic applications, as this morphology reduces heat dissipation and promotes degradation. A ZT of 0.055 was recorded at 501 K in the thin film material and we have fabricated the first reported SnSe-based thermoelectric device with a measurable output of up to $0.09 \mu\text{W}$ at 618 K on the hot side. This work represents an important first step on the route to thin film and/or printed SnSe-based thermoelectric devices, which with high porosity open the possibility of self-powered sensors. The focus must now be on improving electrical conductivity while maintaining the ultralow thermal conductivity of the SnSe thin films to increase ZT values.

Experimental Section

Thin Film Fabrication: Glass substrates were cut into $22 \text{ mm} \times 11 \text{ mm}$ pieces and initially cleaned using a mixture of liquid detergent, Helmanex, and deionized water, before being further washed in

deionized water, acetone, and isopropyl alcohol. Finally, they were plasma cleaned for 15 min. The cleaned glass substrates were loaded into a custom holder for thermal evaporation. Thermal evaporation was performed using an Edwards 306 thermal evaporator, with a tungsten wire holder held in an alumina crucible (Kurt J. Lesker). 0.1 g SnSe powder (0.506 mmol , Sigma-Aldrich, 99.995%) was weighed into an empty alumina crucible prior to evaporation. The 19.6 L evaporation chamber was evacuated to a pressure of $4 \times 10^{-5} \text{ Torr}$, resulting in $1.05 \times 10^{-8} \text{ mmol}$ of oxygen being present in the chamber. Glass substrates were held 17 cm away from the crucible.

Characterization: Silver conductive paint (Electrolube) was used to allow top and bottom contacts to be made (see Figure S1 in the Supporting Information). The Seebeck and electrical measurements were conducted on a ULVAC ZEM-3 in a helium atmosphere. Thermal conductivity was performed using the 3-omega Völklein method with a Linseis Thin Film Analyzer.^[48–50] Samples were prepared by thermal evaporation of SnSe onto prepatterned test chips (Linseis Messgeraete GmbH).^[49] The silicon test chips have a surface termination of silicon nitride, then aluminum oxide. Thermal conductivity measurements were made in an area where the silicon substrate was etched away to leave a $\text{SiN}/\text{Al}_2\text{O}_3$ membrane $\approx 130 \text{ nm}$ thick, and the measurement was in-plane. Where electronic thermal conductivity, κ_e , values were presented, these were determined by the Wiedemann–Franz law ($\kappa_e = L \cdot \sigma \cdot T$, with $L = 1.5 \times 10^{-8} \text{ V}^2 \text{ K}^{-2}$) and the lattice thermal conductivity κ_l was determined by $\kappa_l = \kappa - \kappa_e$.^[13,51]

XRD was performed on a Bruker D8 diffractometer with $\text{Cu K}\alpha$ radiation. SEM and EDX were performed on a Joel 7800F FEG SEM with an oxford laboratory EDX attachment.

XPS was carried out using a Kratos Axis Supra (Kratos Analytical) using a monochromated $\text{Al K}\alpha$ source. Samples were mounted with electrical connection to metallic silver. Due to the differential charging of adventitious carbon, the silver $3d_{5/2}$ peak at 368.2 eV was chosen as a charge reference. High resolution scans with a pass energy of 20 eV and 0.1 eV step size were recorded based on survey scans with a resolution of 160 eV . All data were analyzed on CasaXPS (2.3.17dev6.4k) using the Kratos sensitivity factor library.

Isothermal nitrogen adsorption measurements were performed on a Micromeritics TriStar II at 77 K , prior to measurement samples were degassed with N_2 at $300 \text{ }^\circ\text{C}$ for 20 h .

A Netzsch 404 F1 Pegasus – high-temperature simultaneous thermal analysis (STA) was used to determine the DSC and thermogravimetric analysis (TGA) signals from the sample. The experiment was performed under Argon cover gas using alumina crucibles and using a platinum sample carrier. The samples were heated from 308 to 373 K and then held for 10 min in an isothermal step. The samples were then heated to 600 K at a constant rate of 5 K min⁻¹. The difference in heat flux of each sample was measured against a reference (empty alumina crucible) while being heated at a constant rate (5 K min⁻¹) and the mass of the sample was measured simultaneously.

Device Fabrication: Unless otherwise stated, all conditions used were the same as thin film fabrication. Onto glass substrates measuring 7.5 cm × 2.5 cm, 8 parallel SnSe legs measuring 2.0 cm × 0.2 cm separated by 0.6 cm were evaporated through the first shadow mask. Following this, a second shadow mask was used to evaporate 8 identical Ag legs shifted 0.4 cm across. This mask also created 0.2 cm × 0.6 cm wide Ag contacts to complete the device.

Supporting Information

Supporting Information is available from the Wiley Online Library or from the author.

Acknowledgements

The authors wish to thank EPSRC (EP/N020863/1) for funding. M.C. and A.P. wish like to thank Welsh European Funding Office (SPARC II) for funding. O.C. would like to thank the Royal Society University Research Fellowship (UF140372) for funding. T.L. would like to thank Chinese Scholarship Council for funding. The authors would also like to acknowledge the assistance provided by the Swansea University AIM Facility which is funded in part by EPSRC (EP/M028267/1), European Regional Development Fund via the Welsh Government (80708) and Ser Solar.

All data created during this research are openly available from the Swansea University data archive at <https://doi.org/10.5281/zenodo.1183671>.

Conflict of Interest

The authors declare no conflict of interest.

Keywords

nanosheets, thermal conductivity, thermoelectrics, thin films, tin selenide

Received: February 28, 2018

Revised: April 26, 2018

Published online: June 21, 2018

- [1] J. Besseling, H. Pershad, *The Potential for Recovering and Using Surplus Heat from Industry Final Report*, Department of Energy & Climate Change, London, UK **2014**.
- [2] DEFRA, *Act on CO₂ Calculator: Public Trial Version Data, Methodology and Assumptions Paper*, Department for Environment, Food and Rural Affairs, London, UK **2007**.
- [3] L. E. Bell, *Science* **2008**, 321, 1457.
- [4] R. Venkatasubramanian, E. Siivola, T. Colpitts, B. O'Quinn, *Nature* **2001**, 413, 597.

- [5] A. F. Joffe, L. S. Stil'bans, *Rep. Prog. Phys.* **1959**, 22, 306.
- [6] G. J. Snyder, E. S. Toberer, *Nat. Mater.* **2008**, 7, 105.
- [7] D. A. Wright, *Nature* **1958**, 181, 834.
- [8] L. D. Hicks, M. S. Dresselhaus, *Phys. Rev. B* **1993**, 47, 16631.
- [9] L. D. Hicks, M. S. Dresselhaus, *Phys. Rev. B* **1993**, 47, 12727.
- [10] C. J. Vineis, A. Shakouri, A. Majumdar, M. G. Kanatzidis, *Adv. Mater.* **2010**, 22, 3970.
- [11] M. Zebarjadi, K. Esfarjani, M. S. Dresselhaus, Z. F. Ren, G. Chen, *Energy Environ. Sci.* **2012**, 5, 5147.
- [12] *CRC Handbook of Chemistry and Physics* (Ed: D. R. Lide), CRC Press, Boca Raton, FL, USA **2005**.
- [13] L.-D. Zhao, S.-H. Lo, Y. Zhang, H. Sun, G. Tan, C. Uher, C. Wolverton, V. P. Dravid, M. G. Kanatzidis, *Nature* **2014**, 508, 373.
- [14] L.-D. Zhao, G. Tan, S. Hao, J. He, Y. Pei, H. Chi, H. Wang, S. Gong, H. Xu, V. P. Dravid, C. Uher, G. J. Snyder, C. Wolverton, M. G. Kanatzidis, *Science* **2016**, 351, 141.
- [15] A. T. Duong, V. Q. Nguyen, G. Duvjir, V. T. Duong, S. Kwon, J. Y. Song, J. K. Lee, J. E. Lee, S. Park, T. Min, J. Lee, J. Kim, S. Cho, *Nat. Commun.* **2016**, 7, 13713.
- [16] S. Sassi, C. Candolfi, J.-B. Vaney, V. Ohorodniichuk, P. Masschelein, A. Dauscher, B. Lenoir, *Appl. Phys. Lett.* **2014**, 104, 212105.
- [17] X. Shi, Z.-G. Chen, W. Liu, L. Yang, M. Hong, R. Moshwan, L. Huang, J. Zou, *Energy Storage Mater.* **2018**, 10, 130.
- [18] T.-R. Wei, G. Tan, X. Zhang, C.-F. Wu, J.-F. Li, V. P. Dravid, G. J. Snyder, M. G. Kanatzidis, *J. Am. Chem. Soc.* **2016**, 138, 8875.
- [19] Y. Li, X. Shi, D. Ren, J. Chen, L. Chen, *Energies* **2015**, 8, 6275.
- [20] Y. Fu, J. Xu, G.-Q. Liu, J. Yang, X. Tan, Z. Liu, H. Qin, H. Shao, H. Jiang, B. Liang, J. Jiang, *J. Mater. Chem. C* **2016**, 4, 1201.
- [21] Y. Li, F. Li, J. Dong, Z. Ge, F. Kang, J. He, H. Du, B. Li, J.-F. Li, *J. Mater. Chem. C* **2016**, 4, 2047.
- [22] J. O. Morales Ferreira, D. E. Diaz-Droguett, D. Celentano, J. S. Reparaz, C. M. Sotomayor Torres, S. Ganguli, T. Luo, *Appl. Therm. Eng.* **2017**, 111, 1426.
- [23] C.-L. Chen, H. Wang, Y.-Y. Chen, T. Day, G. J. Snyder, *J. Mater. Chem. A* **2014**, 2, 11171.
- [24] E. K. Chere, Q. Zhang, K. Dahal, F. Cao, J. Mao, Z. Ren, *J. Mater. Chem. A* **2016**, 4, 1848.
- [25] C. H. Suen, D. Shi, Y. Su, Z. Zhang, C. H. Chan, X. Tang, Y. Li, K. H. Lam, X. Chen, B. L. Huang, X. Y. Zhou, J.-Y. Dai, *J. Mater.* **2017**, 3, 293.
- [26] H. Ju, K. Kim, D. Park, J. Kim, *Chem. Eng. J.* **2018**, 335, 560.
- [27] J. Tang, H.-T. Wang, D. H. Lee, M. Fardy, Z. Huo, T. P. Russell, P. Yang, *Nano Lett.* **2010**, 10, 4279.
- [28] Y. Zhang, T. Day, M. L. Snedaker, H. Wang, S. Krämer, C. S. Birkel, X. Ji, D. Liu, G. J. Snyder, G. D. Stucky, *Adv. Mater.* **2012**, 24, 5065.
- [29] X. Chen, A. Weathers, A. Moore, J. Zhou, L. Shi, *J. Electron. Mater.* **2012**, 41, 1564.
- [30] R. Indirajith, M. Rajalakshmi, R. Gopalakrishnan, K. Ramamurthi, *Ferroelectrics* **2011**, 413, 108.
- [31] K. S. Urmila, T. A. Namitha, J. Rajani, R. R. Philip, B. Pradeep, *J. Semicond.* **2016**, 37, 93002.
- [32] A. M. Elbreki, M. A. Alghoul, K. Sopian, T. Hussein, *Renewable Sustainable Energy Rev.* **2017**, 69, 961.
- [33] F. K. Lotgering, *J. Inorg. Nucl. Chem.* **1959**, 9, 113.
- [34] S. Brunauer, P. H. Emmett, E. Teller, *J. Am. Chem. Soc.* **1938**, 60, 309.
- [35] E. P. Barrett, L. G. Joyner, P. P. Halenda, *J. Am. Chem. Soc.* **1951**, 73, 373.
- [36] S. Badrinarayanan, A. B. Mandale, V. G. Gunjekar, A. P. B. Sinha, *J. Mater. Sci.* **1986**, 21, 3333.
- [37] Y. Li, B. He, J. P. Heremans, J.-C. Zhao, *J. Alloys Compd.* **2016**, 669, 224.
- [38] R. B. Shalvoy, G. B. Fisher, P. J. Stiles, *Phys. Rev. B* **1977**, 15, 1680.
- [39] A. Naveau, F. Montiel-Rivera, E. Guillon, J. Dumonceau, *Environ. Sci. Technol.* **2007**, 41, 5376.

- [40] Y. Huang, C. Wang, X. Chen, D. Zhou, J. Du, S. Wang, L. Ning, *RSC Adv.* **2017**, *7*, 27612.
- [41] R. Guo, X. Wang, Y. Kuang, B. Huang, *Phys. Rev. B* **2015**, *92*, 115202.
- [42] I. Sumirat, Y. Ando, S. Shimamura, *J. Porous Mater.* **2006**, *13*, 439.
- [43] G. C. McIntosh, A. B. Kaiser, *Curr. Appl. Phys.* **2001**, *1*, 145.
- [44] T. Hübert, L. Boon-Brett, V. Palmisano, M. A. Bader, *Int. J. Hydrogen Energy* **2014**, *39*, 20474.
- [45] P. J. Taroni, G. Santagiuliana, K. Wan, P. Calado, M. Qiu, H. Zhang, N. M. Pugno, M. Palma, N. Stingelin-Stutzman, M. Heeney, O. Fenwick, M. Baxendale, E. Bilotti, *Adv. Funct. Mater.* **2017**, *28*, 1704285.
- [46] F. Yang, S. Zheng, H. Wang, W. Chu, Y. Dong, *J. Micromech. Microeng.* **2017**, *27*, 55005.
- [47] P. Fan, Z. Zheng, Y. Li, Q. Lin, J. Luo, G. Liang, X. Cai, D. Zhang, F. Ye, *Appl. Phys. Lett.* **2015**, *106*, 73901.
- [48] F. Völklein, *Thin Solid Films* **1990**, *188*, 27.
- [49] V. Linseis, F. Völklein, H. Reith, P. Woias, K. Nielsch, *J. Mater. Res.* **2016**, *31*, 3196.
- [50] V. Linseis, F. Völklein, H. Reith, K. Nielsch, P. Woias, *Rev. Sci. Instrum.* **2018**, *89*, 15110.
- [51] H.-S. Kim, Z. M. Gibbs, Y. Tang, H. Wang, G. J. Snyder, *APL Mater.* **2015**, *3*, 41506.